

## Supplementary Materials

### **Pulsed Dipolar Spectroscopy Reveals that Tyrosyl Radicals are generated in Both Monomers of the Cyclooxygenase-2 Dimer.**

Benjamin J. Orlando<sup>1,‡</sup>, Peter P. Borbat<sup>2,3,‡</sup>, Elka R. Georgieva<sup>2,3,‡</sup>, Jack H. Freed<sup>2,3</sup>, and Michael G. Malkowski<sup>1,4,\*</sup>

<sup>1</sup>Department of Structural Biology, The State University of New York at Buffalo, Buffalo, NY 14203, USA; <sup>2</sup>National Biomedical Center for Advanced Electron Spin Resonance Technology, Cornell University, Ithaca, NY, USA; <sup>3</sup>Department of Chemistry and Chemical Biology, Cornell University, Ithaca, NY, USA; <sup>4</sup>Hauptman-Woodward Medical Research Institute, Buffalo, NY 14203, USA.

This supplement contains:

Supplemental Methods  
Figures S1-S7

## SUPPLEMENTAL METHODS

*Protein expression and purification* – Y385F and Y504F mutant constructs were generated using the QuikChange II site-directed mutagenesis kit (Stratagene) and human (hu) COX-2 in pFastbac1 as the template <sup>1</sup>. All three constructs were expressed in insect cells as previously described <sup>1</sup>. Cell pellets were re-suspended in 50mM Tris, pH 8.0, 300mM NaCl, 1mM  $\beta$ -ME, 10mM imidazole and lysed using a Microfluidizer. Tween-20 was added to the resulting lysate to a final concentration of 1% (v/v) and COX-2 was solubilized from membranes by stirring at 4°C for 1hr. Samples were centrifuged at 40,000 RPM in a Beckman Ti-45 rotor for 1hr at 4°C to remove insoluble material. The resulting supernatant was loaded onto a 5mL Hi-Trap chelating Ni-NTA column (GE Healthcare). The column was washed with buffer A (50mM Tris pH 8.0, 300mM NaCl, 1mM  $\beta$ -ME, 75mM imidazole, 0.1% tween-20 (v/v)) to remove non-specifically bound contaminants before eluting COX-2 with buffer A containing 250mM imidazole. COX-2 containing elution fractions were pooled and dialyzed overnight against 50mM Tris pH 8.0, 300mM NaCl, 0.1% tween-20 (v/v). The dialyzed sample was concentrated to ~4 mg/mL monomer and then trypsin digested at a 30:1 ratio of COX-2 monomer to trypsin for 45 minutes at room temperature. Following limited proteolysis, the trypsin was inhibited by the addition of PMSF to a final concentration of 2mM. The sample was then subjected to size-exclusion chromatography on a HiPrep 16/60 Sephacryl S300 HR column (GE Healthcare) in 25mM Tris pH 8.0, 150mM NaCl, 0.1% tween-20 (v/v). COX-2 containing fractions were pooled and concentrated to 10.5mg/mL (150 $\mu$ M) COX-2 monomer. Concentrated samples were flash frozen in liquid nitrogen and stored at -80°C until further use.

*Purification of 15-HPETE* – The lipid peroxide 15-hydroperoxyeicosatetraenoic acid (15-HPETE) was generated and purified using the method previously described by Graff et al. <sup>2</sup>. Briefly, 13.5 $\mu$ mol of arachidonic acid in ethanol was dispensed into 30mL of 50mM Tris-HCL, pH 9.0 in a 125mL baffled Erlenmeyer flask at 30°C. The reaction flask was vigorously stirred in order to avoid depletion of oxygen during the enzymatic reaction. Oxygenation reactions were initiated by addition of 86.5 Kunits of purified soybean 15-lipoxygenase (Cayman Chemicals) to the flask. The reaction was allowed to proceed for two minutes at 30°C before a second addition of 86.5 Kunits of soybean 15-lipoxygenase and a final 8 minute incubation at 30°C. Reactions were stopped by addition of 7.5mL of ethanol and cooling the flask to 4°C. The reaction mixture was acidified to pH 3.0 and then applied to a pre-washed 6mL C-18 column (J.T. Baker). The column was washed sequentially with 25mL of 20% ethanol, 50mL of water, and 10mL of hexane before eluting 15-HPETE with 10mL of methanol. The methanol was evaporated under a stream of nitrogen and 15-HPETE was re-suspended in ethanol to a final concentration of ~34mM as determined by UV/Vis absorption spectroscopy using a molar extinction coefficient of  $\epsilon_{236}=27,000 \text{ M}^{-1}\text{cm}^{-1}$ . Samples were stored in screw cap amber vials under nitrogen at -80°C until further use.

*UV/VIS Titration with heme* - Titrations of huCOX-2 with heme were carried out as described in <sup>3</sup>. huCOX-2 in 25mM Tris, pH 8.0, 150mM NaCl, 0.53%  $\beta$ OG and at a concentration of 5 $\mu$ M monomer was titrated with Fe<sup>3+</sup>-protoporphyrin IX (Frontier Scientific) and the difference absorption spectra 409nm was recorded (**Fig. S3**).

*DQC data collection and processing* - 150 $\mu$ M huCOX-2 monomer was complexed with 225 $\mu$ M Fe<sup>3+</sup>-protoporphyrin IX and glycerol was added to a final concentration of 20% (v/v). The holo-enzyme was reacted with 1.5mM 15-HPETE on ice for 10s for Y385F and Y504F huCOX-2 and 20s for wild-type huCOX-2 to generate tyrosyl radicals before flash freezing in liquid nitrogen. Double-quantum coherence (DQC) measurements were performed at 17.3GHz and 5K on a home-built pulse ESR spectrometer<sup>4,5</sup> equipped with the 64 step DQC phase cycle suppressing all unwanted coherences up to 6<sup>th</sup> order<sup>6</sup>. A 6-pulse DQC sequence of  $\pi/2-t_p-\pi-t_p-\pi/2-t_d-\pi/2-t_d-\pi/2-(t_m-t_p)-\pi/2-(t_m-t_p)$ -echo, with short 6ns  $\pi$ -pulses with B<sub>1</sub> of 30G was used<sup>7</sup>. For large distances (>40Å) between tyrosyl radicals located in opposite monomers of COX-2, the sampling period ( $t_m$ ) was set as large as possible. Short phase memory time ( $T_m$ ) was partly offset by fast  $T_1$  that results from the close proximity of all tyrosyl radicals to the fast-relaxing iron in heme, thus enabling repetition rates as high as 4kHz. This was essential, since the DQC signal was a small fraction of the primary echo due to noticeably less than quantitative radical yield. By the time of detection, primary echo (and respectively DQC signal) decay by a factor of 500-1500 was encountered, leading to long averaging times from a few hours to several days in the case of  $t_m=3.5 \mu$ s needed for wild type enzyme.

*DQC data processing for long distances* - Acquired DQC time-domain data were processed into distance distributions using Tikhonov regularization and maximum entropy refinement<sup>8,9</sup>. Usually, there is only a small background present in DQC, allowing the data to be converted into distances without background subtraction (**Fig. S4**). In some cases increased background is caused by the limited yield of trapped radicals, resulting in “labeling efficiency” of ~0.15 and consequently to a relatively larger contribution from intermolecular DQC. This intermolecular

contribution gives rise to a practically linear, typically small background contribution (**Fig. S5**). Normally L-curve Tikhonov standard processing uses the first derivative in the regularization term (blue peak in **Fig. S5**). To reduce data smoothing, and thereby increase resolution somewhat, the solution norm may be used instead<sup>9</sup> at the expense of higher noise, particularly at shorter distances (green peaks in **Fig. S5**). This approach was used to better reveal the shape of the distance distribution for wild type COX-2, where 3 long distances, confined to a limited range, have to be distinguished.

The regularization package [http://www.acert.cornell.edu/index\\_files/acert\\_resources.php](http://www.acert.cornell.edu/index_files/acert_resources.php) as used for data with wild type COX-2 had solution norm in the regularization term, rather than the first derivative, thereby avoiding  $P(r)$  over-smoothing by finding the true corner of the L-curve, which is not otherwise reached due to noisy data<sup>9</sup>. This, however, led to noisy features for distances below  $\sim 35\text{\AA}$  (**Fig. 3E and Fig. S4**). The limited distance range from  $37\text{\AA}$  to  $77\text{\AA}$  was used to fit the  $P(r)$  of interest, as no distances were expected to be present outside this range. Note that the widths of reconstructed components may vary, but their areas are substantially invariant, representing the amplitudes of components in the time domain data.

Gaussian fittings were performed using the non-linear least-square curve-fitting algorithm built into OriginLab software (OriginLab, Inc.). To make this procedure more tractable, several manual adjustments were performed before parameters were bounded for final automatic iterations. As initial distance estimates, we used distances connecting Tyr-504 and Tyr-385 ring centers in the COX-2 crystal structure<sup>10</sup>. The three distances Tyr-385•Tyr-385, Tyr-385•Tyr-504, and Tyr-504•Tyr-504 are  $44.6\text{\AA}$ ,  $51.2\text{\AA}$ , and  $59\text{\AA}$ , respectively. Since radical yield ( $f$ ) was estimated as  $\sim 15\%$ , we introduced site occupancies  $f_1 \equiv fp$  and  $f_2 \equiv fq$  for radicals Tyr-385• (short distance) and Tyr-504• (long distance), respectively. As the DQC signal is a sum

of product terms, weights ( $w_1$ ,  $w_2$ ,  $w_3$ ) of Tyr-385•-Tyr-385•, Tyr-385•-Tyr-504•, and Tyr-504•-Tyr-504• in the signal are  $p^2$ ,  $2pq$ , and  $q^2$ . After several trials around seeded values, they were bounded and the widths were fit. Finally, all Gaussian parameters were fit simultaneously within narrow bounds of  $\pm 1$  Å. The best fit was obtained for  $p = 0.68$ , with Gaussian mean values of 43.4Å, 52Å, and 59Å, and standard deviations of 2.6Å, 4.6Å, and 7Å, respectively (**Fig. S6**). Occupancy,  $p$  (or  $q$ ) is a rather stable parameter, as distribution shape conforms to it. We note that the trimmed off intra-monomer Tyr-385-Tyr-504 component should have had the same weight  $w_2=0.44$  as the inter-monomer Tyr-385-Tyr-504 component. This is indeed the case, as we find it to be  $\sim 0.5$ , which is well within the expected range of uncertainty. Even without performing data fitting the prominence of the Tyr-385•Tyr-385 distance, rather than the Tyr-385•Tyr-504 radical distance, and the weakness of the Tyr-504•Tyr-504 radical distance are strong indicators of the Tyr-385 radical being more abundant. We can obtain a slightly better fit by releasing the weight constraints, but it is clear that higher signal-to-noise and longer time-scale data are needed to address such details. Given the low intensity of the longest distance (Tyr-504•Tyr-504), the modeling could consider a fit to two Gaussians. When this type of fit was performed the second component became broad and dominates with a 78% fraction, indicating an abundance of Tyr-504•Tyr-504, which is not consistent with our data.

The primary reason for the inability to clearly resolve the longest distance (Tyr-504•Tyr-504; **Fig. 3C**) is due to the relative weakness of this component and an insufficient time interval ( $t_m$ ) for signal sampling. The limitation was due to the short phase memory time ( $T_m$ ) for all the radicals. This is expected given the hydrophobic environment of the protein interior<sup>11</sup>, with  $T_m$ 's shortened further for radicals in proximity to the fast-relaxing iron ion within the heme moiety (9-13Å), necessitating the measurements be conducted at a temperature of 5K. Even at 5K, very

fast primary echo decays were recorded with  $T_m$ 's in the range of 0.8-1  $\mu$ s, thus limiting the achievable  $t_m$ 's to 2.5-3.5  $\mu$ s. The decay of the echo by time  $t_m$  was typically a factor of  $\sim$ 1500 in these measurements. Furthermore, the achievable radical yield reduced the percentage of protein molecules contributing to the dipolar signals, making this case very demanding on the method used. The ability to average the signal over a reasonable period of time was helped by short  $T_1$ 's of all radicals, permitting a 4kHz pulse repetition rate at 5K. This also indicated that all radicals are in the proximity of fast relaxing iron ion within the heme moiety.

*DQC data processing for the short intra-monomer Tyr-385•Tyr-504 Distance* - Tikhonov regularization based on an ideal (secular) kernel produced a distance distribution with contributions in the range of 10.2-14.6Å and an average distance of 12.4Å, with a maximum at  $\sim$ 11.2Å. This is very close to the 12.25Å average distance calculated from the crystal structure of COX-2, taking into account the distances between ring carbons, beta-carbon and oxygen ranging from 10.1Å to 14.6Å. This excellent agreement is possible because down to  $\sim$ 10Å, the pseudosecular term is not dominant for 20G FWHM spectrum and 30G  $B_1$  microwave pulses; therefore error in distance from this source is a fraction of an angstrom. At this separation ( $>$ 10Å), through space exchange interaction can generally be ignored<sup>12-14</sup>. We find that the fit is slightly improved when small (-2.2 MHz)  $J$  was employed (**Fig. S7**).

Figure S1

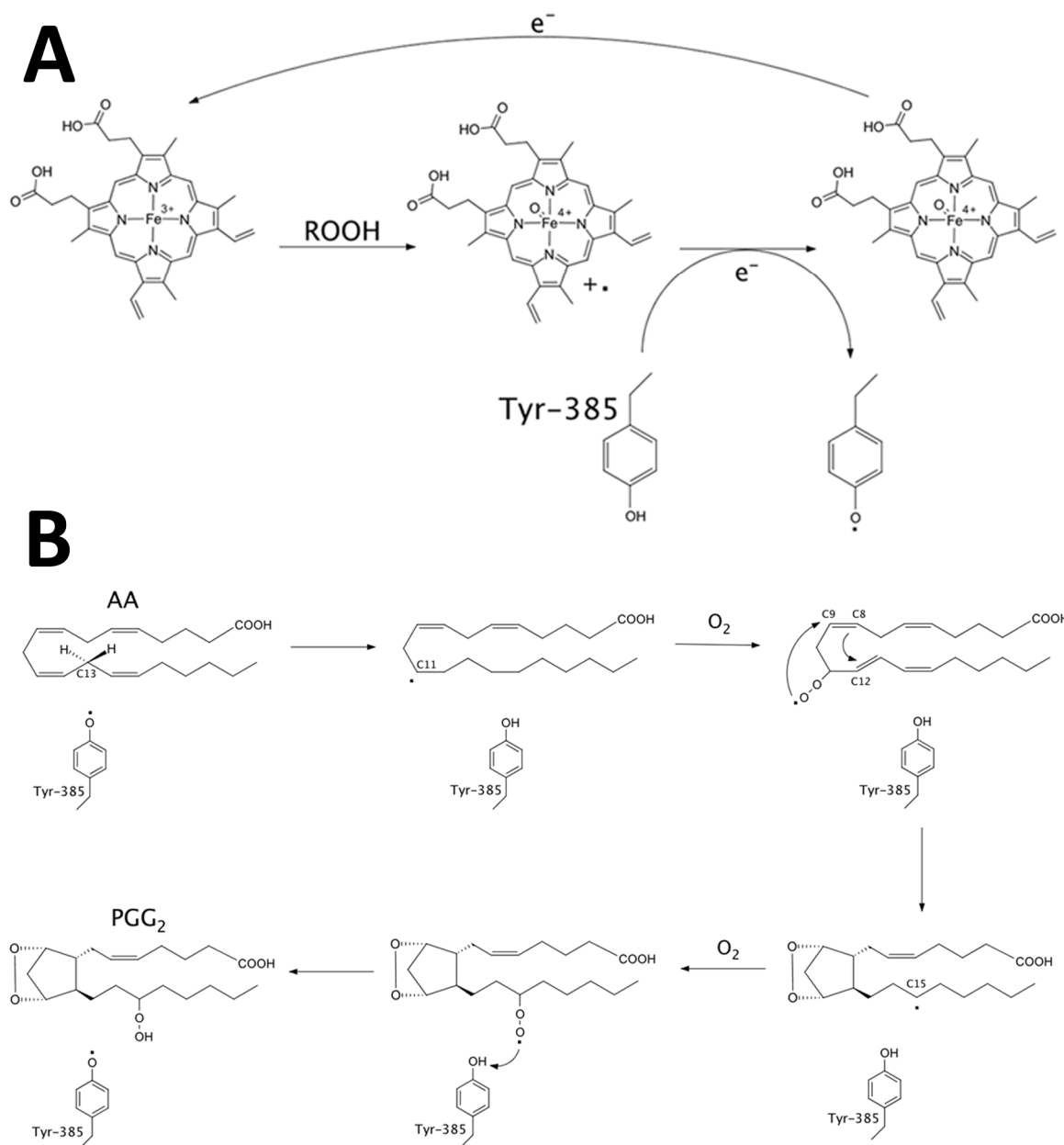


**Figure S1. COX-2 Catalytic Reaction Mechanisms. (A)** In the resting state COX-2 contains a  $\text{Fe}^{3+}$ -Protoporphyrin IX group in the peroxidase active site. Reaction with peroxide oxidizes the heme to a ferryl-oxo protoporphyrin cation radical. Electron transfer from Tyr-385 reduces the porphyrin cation radical while concurrently generating a Tyr-385 radical in the cyclooxygenase active site. Reducing co-substrates such as phenol induce a further single electron reduction of the ferryl-oxo heme back to the ferric resting state. **(B)** The Tyr-385 radical generated by the peroxidase reaction abstracts the 13-pro-*S* hydrogen from AA, generating an AA radical. Molecular oxygen reacts preferentially with the radical on carbon-13 of AA to form a carbon-11 peroxy radical, which then cyclizes to form an endoperoxide bridge between carbon-11 and carbon-9 of AA, and cyclopentane ring closure between carbon-8 and carbon-12, generating a carbon-15 centered radical. A second molecule of oxygen reacts with the carbon-15 radical to form a 15-peroxy radical. Finally, the hydrogen that was abstracted by Tyr-385 is donated back to the 15-peroxy radical to form  $\text{PGG}_2$ , and regenerate the catalytic Tyr-385 radical.

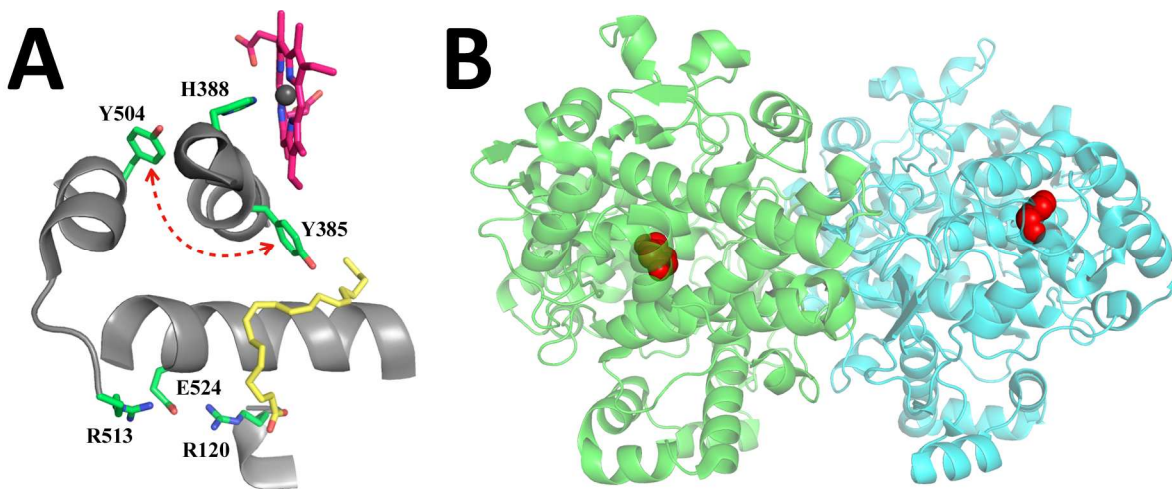


**Figure S2. Tyrosyl Radical Equilibrium and Half-of-Sites Reactivity.** (A) A schematic depicting the spatial relationship between Tyr-385, Tyr-504, and the heme moiety in a monomer of COX-2. AA (yellow) is bound in the cyclooxygenase channel, with carbon-13 located below the phenolic oxygen of Tyr-385. The proximal histidine (H388) and residues at the opening of the cyclooxygenase active site (R120, R513, and E524) are labeled accordingly. Tyrosyl radicals are formed on Tyr-385 and Tyr-504 following the reaction of COX-2 with a peroxide substrate. Previous cw-ESR studies propose that a radical equilibrium exists with reversible electron transfer between Tyr-385 and Tyr-504, with Tyr-504 serving as a “radical reservoir” that can replenish the catalytic Tyr-385 radical upon depletion by reductant <sup>15</sup>. (B) A hypothetical scenario to describe half-of-sites reactivity observed in COX-2. Reaction with peroxide generates tyrosyl radicals on Tyr-385 in one monomer and Tyr-504 in the partner monomer. The monomer containing the Tyr-385 radical is designated as the catalytic monomer (green), whereas the Tyr-504 radical containing monomer is catalytically inactive (blue). Tyr-385 and Tyr-504 are shown with red spheres.

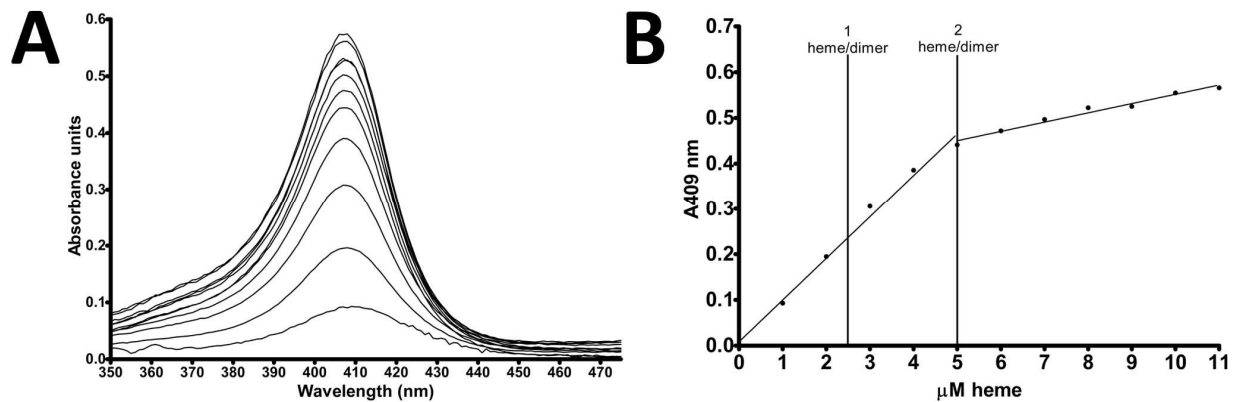


**Figure S3. UV/Vis Titration of COX-2 with  $\text{Fe}^{3+}$ -Protoporphyrin IX.** huCOX-2 ( $5\mu\text{M}$  monomer) in 25mM Tris, pH 8.0, 150mM NaCl, 0.53% (v/v)  $\beta\text{OG}$  was titrated with  $\text{Fe}^{3+}$ -protoporphyrin IX and difference absorption spectra were recorded at each concentration of heme. **(A)** Increase in Soret peak absorbance at 409nm following the binding of heme to huCOX-2. **(B)** Plot of the increase in absorbance at 409nm versus heme concentration. The increase in absorbance was linear up to  $5\mu\text{M}$  heme, indicating that heme binds to both monomers of the huCOX-2 dimer.

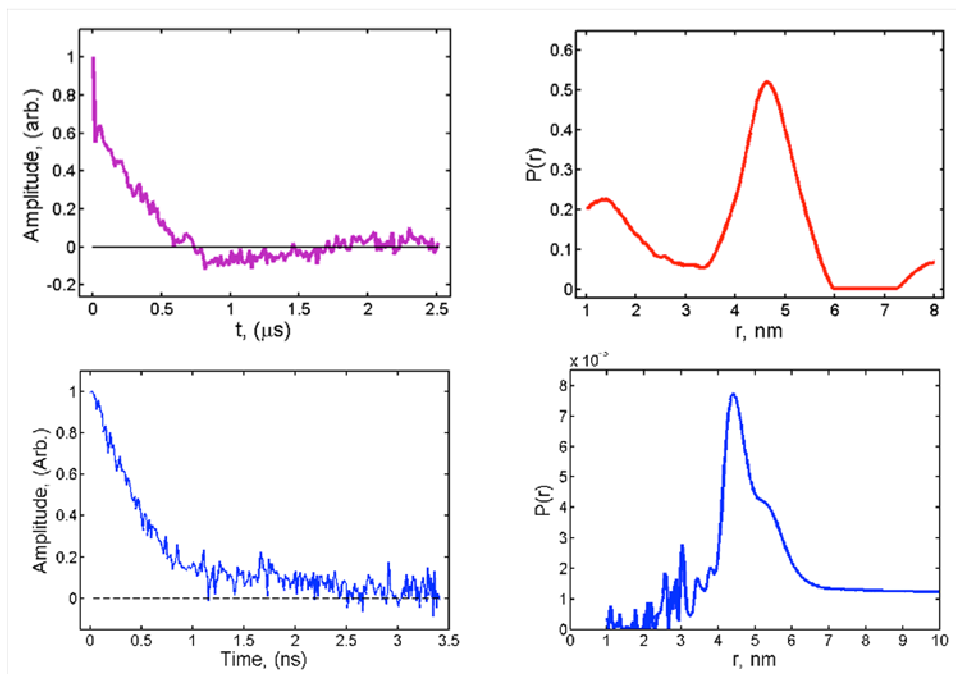


**Figure S4. DQC Data Collection and Processing for Long Distances in Wild Type COX-2.**

*Top Left* – The DQC signal for wild type huCOX-2, with both Tyr-385 and Tyr-504 radicals generated, was recorded using  $t_m=2.5\mu\text{s}$  in 8h. *Top Right* – Reconstruction of the data on the left was performed using the first derivative in L-curve regularization and maximum entropy refinement. The short distance in the beginning of the time-domain data reconstructs as a broad line (compare with **Fig. 3E** in the main text). The longer distance lines in the center are unresolved, but they become resolved when there is less smoothing of the data, as illustrated in the bottom row. *Bottom Left* – The DQC signal for wild type huCOX-2, with both Tyr-385 and Tyr-504 radicals present, was acquired using  $t_m=3.5\mu\text{s}$ . The short-distance signal was removed and the background was left as is. *Bottom Right* – Reconstruction was performed first with L-curve Tikhonov regularization not using derivative and then was subjected to maximum entropy refinement. Beyond  $\sim 37\text{\AA}$ , the signal is clean and reproduces the shape of the spectrum of interest. The background results in moderate “plateau”.

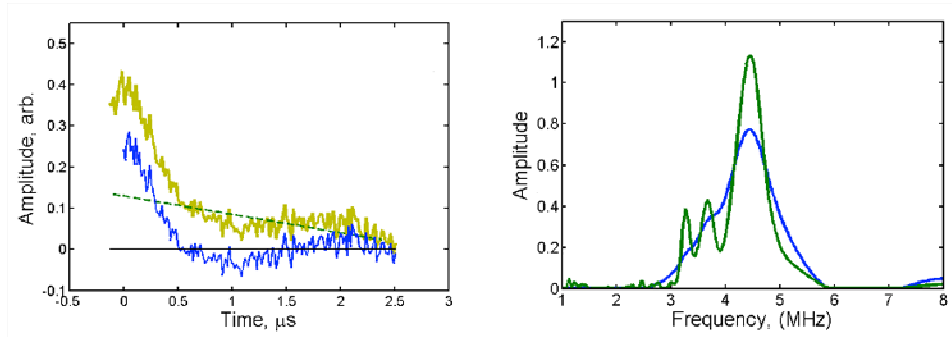


**Figure S5. DQC Data Processing Example of Data Reconstruction for the Tyr-504•Tyr-504 Inter-Monomer Distance in Y385F COX-2.** *Left* – Raw DQC data with linear background fit (dashed green line) and background-free data (blue) after subtraction. *Right* – Tikhonov L-curve reconstruction<sup>9</sup> was used as a seed in subsequent maximum entropy method refinement<sup>8</sup>.

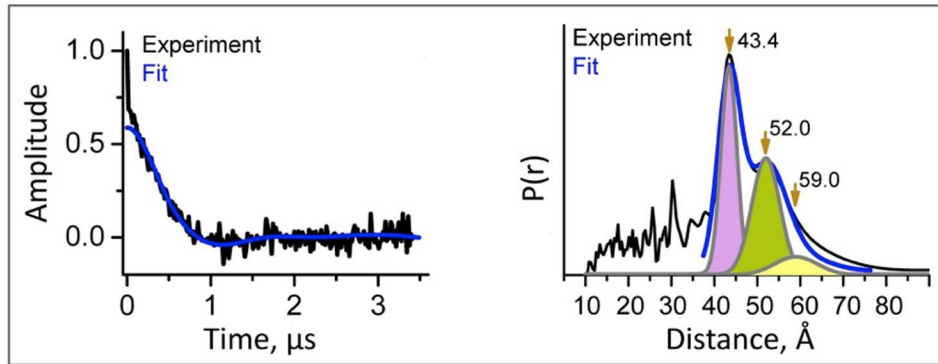


**Figure S6. Gaussian Fit to Wild Type COX-2 Distance Distribution.** *Left panel:* The experimental time-domain DQC signal from tyrosyl radicals in wild type huCOX-2 (black) is plotted together with its fit based on the distance distribution produced by 3-Gaussians fit to the distribution reconstructed from the experimental DQC data (right panel). *Right panel:* DQC derived distance distribution  $P(r)$  of wild type huCOX-2 (black) was generated by L-curve Tikhonov regularization and refined with maximum entropy methods<sup>8,9</sup>. The very short (intra-monomer) distance in the beginning of the record is a single point spike at 32ns dwell time used. This single point was trimmed off prior to distance reconstruction, leaving only the task to estimate three remaining long inter-monomer distances.  $P(r)$  was fit to a model based on the weighted sum of three Gaussians resulting in the distribution plotted in blue.

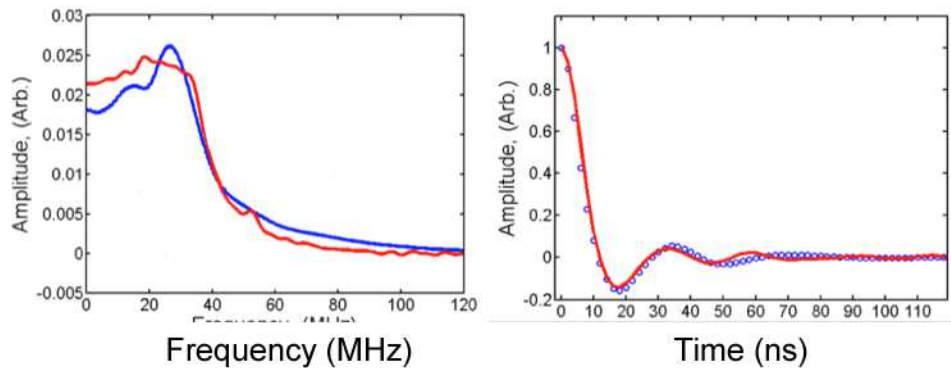


**Figure S7. Comparison of Simulated and Experimental DQC Data for Tyr-385•Tyr-504 Intra-Monomer Distance.** *Right*–Time-domain DQC data for intra-monomer Tyr-385•Tyr-504 pair (red) and simulated signal (blue circles). The simulations were performed using analytical approximation <sup>16</sup>. The model used 20G FWHM Gaussian envelope for Ku-band Tyrosyl ESR spectrum; each radical was represented by a prolate ellipsoid ( $a=1.5\text{\AA}$ ,  $b=3\text{\AA}$ ) and they were oriented with Euler angles  $\beta_1=0^\circ$  and  $\beta_2=90^\circ$  in the dipolar frame. In accordance with the crystal structure, the distance between centroids, was  $12.3\text{\AA}$ ;  $J=-2.2\text{MHz}$ .  $B_1=30\text{G}$ . *Left*–Dipolar spectrum (half of Pake doublet shown) and its fit based on Fourier-transform of the time-domain simulated data. Note a small peak at  $\sim 52\text{MHz}$  corresponding to nuclear double Zeeman frequency from matrix protons.

## REFERENCES

- [1] Orlando, B. J., McDougle, D. R., Lucido, M. J., Eng, E. T., Graham, L. A., Schneider, C., Stokes, D. L., Das, A., and Malkowski, M. G. (2014) Cyclooxygenase-2 catalysis and inhibition in lipid bilayer nanodiscs, *Arch Biochem Biophys* 546, 33-40.
- [2] Graff, G., Anderson, L. A., and Jaques, L. W. (1990) Preparation and purification of soybean lipoxygenase-derived unsaturated hydroperoxy and hydroxy fatty acids and determination of molar absorptivities of hydroxy fatty acids, *Anal Biochem* 188, 38-47.
- [3] Dong, L., Vecchio, A. J., Sharma, N. P., Jurban, B. J., Malkowski, M. G., and Smith, W. L. (2011) Human cyclooxygenase-2 is a sequence homodimer that functions as a conformational heterodimer, *J Biol Chem* 286, 19035-19046.
- [4] Borbat, P. P., Crepeau, R. H., and Freed, J. H. (1997) Multifrequency two-dimensional Fourier transform ESR: an X/Ku-band spectrometer, *J Magn Reson* 127, 155-167.
- [5] Borbat, P. P., Georgieva, E. R., and Freed, J. H. (2013) Improved Sensitivity for Long-Distance Measurements in Biomolecules: Five-Pulse Double Electron-Electron Resonance, *J Phys Chem Lett* 4, 170-175.
- [6] Gaffney, B. J., Bradshaw, M. D., Frausto, S. D., Wu, F., Freed, J. H., and Borbat, P. (2012) Locating a lipid at the portal to the lipoxygenase active site, *Biophys J* 103, 2134-2144.
- [7] Borbat, P. P., and Freed, J. H. (2013) Pulse Dipolar Electron Spin Resonance: Distance Measurements, In *Structure and Bonding* (Harmer, J., and Timmel, C. R., Eds.), Springer, Berlin.
- [8] Chiang, Y. W., Borbat, P. P., and Freed, J. H. (2005) Maximum entropy: a complement to Tikhonov regularization for determination of pair distance distributions by pulsed ESR, *J Magn Reson* 177, 184-196.
- [9] Chiang, Y. W., Borbat, P. P., and Freed, J. H. (2005) The determination of pair distance distributions by pulsed ESR using Tikhonov regularization, *J Magn Reson* 172, 279-295.
- [10] Vecchio, A. J., Simmons, D. M., and Malkowski, M. G. (2010) Structural basis of fatty acid substrate binding to cyclooxygenase-2, *J Biol Chem* 285, 22152-22163.
- [11] Huber, M., Lindgren, M., Hammarstrom, P., Martensson, L. G., Carlsson, U., Eaton, G. R., and Eaton, S. S. (2001) Phase memory relaxation times of spin labels in human carbonic anhydrase II: pulsed EPR to determine spin label location, *Biophys Chem* 94, 245-256.
- [12] Bittl, R., and Schulten, K. (1990) Biradical Spin Dynamics with Distance-Dependent Exchange Interaction and Electron-Transfer Efficiency, *Chem Phys Lett* 173, 387-392.
- [13] Fiori, W. R., and Millhauser, G. L. (1995) Exploring the peptide 3(10)-helix reversible alpha-helix equilibrium with double label electron spin resonance, *Biopolymers* 37, 243-250.
- [14] Steinhoff, H. J., Radzwill, N., Thevis, W., Lenz, V., Brandenburg, D., Antson, A., Dodson, G., and Wollmer, A. (1997) Determination of interspin distances between spin labels attached to insulin: comparison of electron paramagnetic resonance data with the X-ray structure, *Biophys J* 73, 3287-3298.
- [15] Rogge, C. E., Liu, W., Wu, G., Wang, L. H., Kulmacz, R. J., and Tsai, A. L. (2004) Identification of Tyr504 as an alternative tyrosyl radical site in human prostaglandin H synthase-2, *Biochemistry* 43, 1560-1568.
- [16] Misra, S. K., Borbat, P. P., and Freed, J. H. (2009) Calculation of Double-Quantum-Coherence Two-dimensional Spectra: Distance Measurements and Orientational Correlations., *Applied Magnetic Resonance* 36, 237-258.